

Supporting Information

Alice Lay,^{*,†} Derek S. Wang,[‡] Michael D. Wisser,[‡] Randy D. Mehlenbacher,[‡] Yu Lin,[¶] Miriam B. Goodman,[§] Wendy L. Mao,^{||} and Jennifer A. Dionne^{*,‡}

[†]*Department of Applied Physics, Stanford University, Stanford, CA 94305*

[‡]*Department of Materials Science and Engineering, Stanford University, Stanford, CA 94305*

[¶]*Stanford Institute for Materials and Energy Sciences, SLAC National Accelerator Laboratory, Menlo Park, CA 94025*

[§]*Department of Molecular and Cellular Physiology, Stanford University, Stanford, CA 94305*

^{||}*Department of Geological Sciences, Stanford University, Stanford, CA 94305*

E-mail: alay@stanford.edu; jdionne@stanford.edu

Methods

Cubic-phase nanoparticle synthesis

α -NaYF₄ NPs are synthesized using a modified procedure detailed by Zhang et al.¹ and Tian et al.² In a round bottom flask, 0.3 g of NaOH is dissolved in 1.5 mL deionized water. Then, 5 mL (4435 mg) of 90% oleic acid (Sigma-Aldrich) and 5 mL of ethanol are added under vigorous stirring. Once the mixture is clear and free of solid pieces, 2 mL of 0.2 M aqueous stock solution containing molar ratios of Ln(NO₃)₃ salts (2 mol% Er³⁺, 18 mol% Yb³⁺, and 80-x mol% Y³⁺) and MnCl₂ (x = 0, 3, 5, 10 mol% Mn²⁺) are added. Subsequently, 1 mL of 2 M NH₄F stock solution is added, increasing the turbidity. The resulting mixture is

stirred at room temperature for 20 minutes before being transferred into a 23 mL Teflon-lined autoclave (Parr Instruments, Inc.) and heated in the furnace for 2 hours at 120°C. After the autoclave is naturally cooled to room temperature, the supernatant is removed and the white precipitate is collected with ethanol. Finally, the nanoparticles are washed by centrifugation with ethanol several times before re-suspending in cyclohexane. Thereafter, the colloidal nanoparticles are stored in the refrigerator.

Hexagonal-phase nanoparticle synthesis

β -NaYF₄ NPs are synthesized colloidally through a procedure adapted from Wang et al.³ Briefly, 0.2 M aqueous lanthanide or manganese solutions prepared from acetate and chloride salts, respectively, are mixed in appropriate volumetric ratios to give a total of 2 mL. Nanoparticles are synthesized with 18 mol% Yb³⁺, 2 mol% Er³⁺, 80-x mol% Y³⁺, and x mol% Mn²⁺, with x ranging from 0 to 40 mol%. Upon adding 3 mL oleic acid and 7 mL octa-1-decene, the precursor solution is stirred at 150°C for 40 minutes. Thereafter, we let the mixture cool to room temperature and add 3.3 mL of 0.4 M NH₄F in methanol and 1 mL of 1 M NaOH in methanol. Subsequent stirring at 50°C for 40 minutes induces nuclei formation. Then, the solution is heated at 100°C for ten minutes under vacuum, ensuring that methanol, water, and other contaminants are evaporated. Finally, the solution is heated at 315°C for 90 minutes under Ar gas flow. Once the mixture cools to room temperature, the particles are collected and washed three times in ethanol before re-suspending in cyclohexane.

DAC sample loading

We use a symmetric DAC containing 500 μ m diameter culets to compress the particles up to approximately 3.5 GPa. Prior to sample loading, we pre-indent a stainless steel gasket of an original thickness of 280 μ m to 15 GPa, yielding thicknesses of 30 to 50 μ m, and drill a 300 μ m diameter hole for the sample chamber. Meanwhile, colloidal UCNPs are dropcast on a

glass slide and heated on a hot plate until the solvent evaporates. Flakes of NPs are scraped off using a fine needle-point tool and loaded to fill the sample chamber. Additionally, silicone oil (density of 0.96 g/mL and viscosity of 0.5 Pa·s) is added to maintain a quasi-hydrostatic environment. A ruby ball (tens of microns in size) is loaded for pressure calibration. The ruby PL at ambient pressure is measured before closing the cell and tightening the screws.

DAC measurement of PL and UC

The DAC is secured on a custom-built stage for a Zeiss Axio Observer inverted microscope; it sits in a recessed slot matched to the size and shape of the cell, while two screws in perpendicular directions lock it in place. This setup minimizes the translational and rotational movement of the cell between pressure points. We position the cell using imaging mode on the spectrometer (Princeton Instruments Acton 2500), such that the ruby is located at the center of the CCD detector (Princeton Instruments ProEM eXcelon) and spectrometer slit width set to 250 μm . In this way, we ensure that the same strip of nanoparticles is evaluated throughout a DAC experiment. For each pressure, we find the focus by maximizing the ruby PL intensity under 488nm illumination from an Coherent Innova Argon-ion laser. First, we calibrate the pressure exerted on the loaded NPs. Ruby (Cr^{3+} -doped Al_2O_3) PL spectrum has a characteristic doublet feature, with R_1 and R_2 emission peaks from the crystal field splitting of the radiative Cr^{3+} energy level transition.⁴ The spectra are collected with a 500-Blaze 1800 groove/mm grating, which yields high resolution peaks with an uncertainty of 0.02 nm. The R_1 emission peak is fitted to a Gaussian function, from which the peak wavelength position is determined. This value, λ , is compared to that of the ambient condition, λ_o , in order to calibrate the pressure using the equation:^{5,6}

$$P = (A/B)[(\lambda/\lambda_o)^B - 1] \quad (1)$$

where $A = 1904$ GPa and $B = 7.715$. Given the uncertainty on the calibration equation and 0.02 nm resolution of the grating (~ 0.05 GPa or 100 nN), pressure values are rounded to the tenth decimal place when reported.

An optical image of the gasket is acquired by a digital camera (Allied Vision Technologies) under 488 nm illumination for visualization of PL. For spectra collection, a 684 short-pass (SP) filter is placed below the 488 nm dichroic filter cube to reduce the intensity of ruby PL and prevent the signal from bleeding into that of the NPs. Additionally, we evaluate a region of interest to minimize contributions of ruby PL. In order to capture Er^{3+} emission in the red and green, a 500-Blaze 150 groove/mm grating is used. Similarly, UC spectra and optical images are acquired under 980 nm illumination from a Coherent Ti:Sapphire laser. A 842 SP filter (Semrock BrightLine) is placed at the bottom of the Zeiss brightfield cube to cut off the 980nm source. In this case, we evaluate the full DAC since ruby does not photoluminesce under NIR illumination. The illumination power density is maintained at ~ 90 W/cm² (α -phase) or ~ 50 W/cm² (β -phase) incident on the DAC for 30 sec or 1 sec acquisition times per UC spectra, respectively. Over the course of the experiment, we monitor the laser quality using the optical images and pick-off power values. A polarized beam splitter and half wave plate at the output of the Ti:Sapphire laser source allow us to maintain a similar power for each pressure point. For each pressure point, we iterate the collection of optical images and spectra 3 times in a cyclic fashion, from ruby PL to nanoparticle PL to nanoparticle UC. Data collection is 20-30 min per pressure point, with ~ 15 min wait time between pressure points to allow the pressure (i.e. ruby PL) to reach equilibrium.

Data processing

We integrate signal from the full chip (UC and PL of dropcasted NPs, UC in DAC) or region of interest (PL in DAC) to produce each spectra. For PL spectra of NPs in the DAC, there is a broad background peak from amorphous carbon⁷ that we subtract out. Integrated

intensity and $\frac{I_r}{I_g}$ values are then approximated by Reimman sums over the g_1 , g_2 , and r peaks, using widths of 0.21 nm, the resolution of the 150 groove/mm grating. In Figure 2b, one spectrum is collected per data point, such that errors (within the size of the markers) correspond to the resolution of the spectrometer grating and definition of peak intervals. In DAC measurements, we report the mean pressure and $\frac{I_r}{I_g}$ values of the three spectra collected per ruby, UC, or PL condition. The percent change in the red to green ratio from the undoped (0 % Mn²⁺) or ambient condition, $\frac{I_{ro}}{I_{go}}$, is then calculated using the equation:

$$\Delta \frac{I_r}{I_g} = \left(\frac{I_r/I_g}{I_{ro}/I_{go}} - 1 \right) \cdot 100\% \quad (2)$$

For Figure 3a and 3b, linear least squares fits are performed using Matlab curve-fitting software, with weights designated as the standard deviation of each pressure point and error propagated through the division of the measured $\frac{I_{ro}}{I_{go}}$. Each fit and data set is scaled so that the fitted $\frac{I_{ro}}{I_{go}}$ value is at 0% (Table S6-S9). The error on the slope or pressure sensitivity is taken as half of the 95% confidence interval.

Conversion to force

The total magnitude of force exerted on each nanoparticle is calculated by multiplying pressure with its surface area: $6l^2$ for a cube-like α -NaF₄ nanoparticle and $4\pi r^2$ for a sphere-like β -NaF₄ nanoparticle. Dimensions for edge length (l_o) and radius (r_o) can be found in the TEM particle analysis (see Figure S1). From representative *in situ* XRD experiments (Figure S15) and previous literature,⁸ we derive an average elastic modulus, $E = 272 \pm 2$ GPa, for NaYF₄ nanoparticles. From this material property, we determine the pressure dependence of l and r , defined generally as x :

$$x = (1 - \epsilon)x_o = \left(1 - \frac{\sigma}{E}\right)x_o \quad (3)$$

Here, ϵ is the compressive strain response of the lattice parameter due to applied stress σ . Pressure to force conversions are found in Figure S17.

Chemical composition

Control of the chemical composition is important in isolating the effects of Mn^{2+} on emission and sensing properties, as well as for directly comparing nanoparticles within and between series. To determine true *d*-metal and lanthanide doping concentrations, we utilize inductively-coupled plasma optical emission spectrometry (ICP-OES). Powders of UCNPs ($\sim 1\text{-}5$ mg) are prepared by blowing the solvent off with argon gas flow or allowing the solvent to evaporate in vacuum overnight. With the assumption that 50% of each sample’s measured mass is made of organics (e.g. oleic acid ligand), 10 mg/mL solutions are created with 3% nitric acid and 97% DI water by volume. The sample is fully dissolved in ICP-grade nitric acid before adding water. ICP standards for each element (Y, Yb, Er, Mn) are used to create a “High Standard” (2x maximum expected concentration of each element), “Quality Control” (maximum concentration of each element), and “Blank” (3% nitric acid) standard solutions. The absolute concentration (in ppm) of each element is measured and converted to molar percentages.

In agreement with the findings of Li et al. on $\text{NaGdF}_4\text{:Yb,Tm@NaGdF}_4\text{:Mn}$ core-shell UCNPs,⁹ Mn^{2+} is more easily and consistently incorporated into the cubic (α) lattice than into the hexagonal (β) lattice. As seen in Table S1 and S2, the disparity between “as synthesized” doping amounts compared to actual doping concentrations is larger for $\beta\text{-NaYF}_4$. This disparity may be due to the preference of Mn^{2+} to be in an octahedral complex and symmetry, which is only supported by the $\alpha\text{-NaYF}_4$ lattice.^{10,11} Hence, *d*-metal doping in the β -phase results in greater lattice distortion and requires greater precursor input, as seen in Figure S2. Interestingly, in the α -series, true doping concentrations are consistently about half that of “as synthesized” values. Such reproducibility is an additional benefit of the

α -NPs as a force-sensing tool.

For the film and DAC studies on optical behavior at ambient and high pressure conditions, we utilize specific α -NaYF₄ samples with true Mn²⁺-doping concentrations of 0.0%, 1.7%, 2.8%, and 4.8%. Table S1 summarizes ICP results for all syntheses conducted. Samples with asterisks in Table S2 represent the Mn²⁺-doped samples of the β -series at 0.0%, 0.5%, and 1.5%, which we investigate throughout the main text.

Typically beyond 5% true doping concentrations, another phase (e.g. MnF₄, NaMnF₃) appears and the sensitizer to emitter ratio, Yb/Er, changes significantly. Literature indicates that increased Yb³⁺ suppresses green emission, thereby enhancing the red to green ratio, $\frac{I_r}{I_g}$, by facilitating back energy transfer from Er³⁺ to Yb³⁺.¹² We note that for the β -series, the Yb/Er ratio ranges from 8.3 to 9.5. For the α -series, the ratio ranges from 8.9 to 10.5. These ranges significantly overlap, and while these variations may somewhat contribute to the trend of $\frac{I_r}{I_g}$ in UC (Figure 2), the PL trends should not be affected, since Er³⁺ green states are populated by the excitation source (Figure S13). In PL, enhancements in red emission are seen with increasing Mn²⁺, so we can confirm the coupling of Mn²⁺ to Er³⁺ emission despite these variations.

Particle analysis

Since nanoparticle size has also been shown to impact emission properties including quantum efficiency,¹³ we investigate the size, morphology, and uniformity of our nanoparticles. We aim to achieve as similar physical properties as possible. Micrograph images are obtained with an FEI Tecnai transmission electron microscope (TEM). For an area containing about 150 to 300 nanoparticles, ImageJ software (National Institutes of Health) is implemented to analyze nanoparticle size, either by setting a threshold pixel value or hand-drawing the outline of each nanoparticle. The area is then calculated for each region of interest, from which a length or radius value is derived by assuming a cubic (α -phase) or spherical (β -phase) morphology.

Finally, a histogram of the values is created and fitted to a probability density function, which expresses the likelihood of finding an NP of each size. The mean and standard deviation of the nanoparticles are displayed along with the TEM images in Figure S1. Overall, the β -phase NPs are more monodisperse than the α -phase NPs. However, within the α -series, the size dispersion is relatively constant across all Mn^{2+} -doping concentrations.

Pre-stress structural characterization

X-ray diffraction (XRD) is performed on thin films of samples, prepared by dropcasting the colloiddally suspended NPs on a glass slide. Figure S2a and S2b show the diffraction patterns for the α -series and β -series, respectively. Scans are collected on an X’Pert X-ray diffractometer (PANalytical B.V.) located in the Stanford Nano Shared Facilities (SNSF), using a $\text{Cu K}\alpha_1$ X-ray source ($\lambda = 1.54056 \text{ \AA}$) with 2θ from 10 to 100 degrees.

Across all Mn^{2+} -doping concentrations, the diffraction peaks are consistent with those of the International Centre for Diffraction Data (ICDD) references, indicating that our synthesis procedures yield pure-phase nanoparticles in contrast to previously reported literature.² Here, no additional phase separation steps are required in order to isolate the effect of Mn^{2+} -doping on both α and β crystal lattice structures. In Figure S2a, the additional peak at 39° can be attributed to the optically inert precursor, NaF, while additional peaks at 38° and 41° in Figure S2b can be attributed to the aluminum sample holder.

Lattice constants are derived from the diffraction patterns using a least-squares Pawley¹⁴ fitting routine on the PANalytical HighScore Plus software. α -NPs are constrained to the crystal class $\text{Fm}\bar{3}\text{m}$ and β -NPs to the crystal class P63/m . The fit is performed 5 times per sample for convergence, with residuals or R-values $< 2.5\%$. Table S3 reports the fitted α -lattice constant, a , and β -lattice constants, a and c . The data reveal that increasing doping concentration generally decreases the average lattice parameter, which is consistent with the fact that Mn^{2+} ions (97 pm in high spin ligand field) are smaller in size than Y^{3+} ions (115.9

pm).¹⁵ In Figure 1c, the lattice strain is calculated as the percent change in the constants compared to 0.0% values. The strain of c in β -NPs is highest, indicative of greater lattice distortion caused by d -metal doping in the β - versus α -phase crystal structure.

Laser stability on intensity and color readouts

Since the reported error bars encompass only laser fluctuations during the experimental time for one pressure point (see Methods) and not between pressure points, we perform a laser stability test over 6 to 17 hours prior to each DAC experiment. This procedure allows us to track the quality of the Ti:Sapphire laser, which is susceptible to external changes in temperature and humidity. First, a test sample, usually one from a recently completed DAC experiment, is securely set in place. Then, we follow the collection procedure for a typical DAC measurement (see Methods) without changing pressure. We find that integrated intensity values vary up to $\sim 6\%$ and $\frac{I_r}{I_g}$ values vary up to $\sim 1.5\%$ over time (Figure S4). From these results, we show that the intensity readout is more susceptible to systematic errors than the color readout. In considering the application of these NPs for *in vivo* and *in situ* measurements, where there are often variations in tissue or material thicknesses, a ratiometric quantity like $\frac{I_r}{I_g}$ is most reliable.

Quasi-hydrostatic environment in the DAC

For the pressure range we exert (maximum of 3.5 GPa), we chose to implement 0.5 Pa·s silicone oil, which does not react with our samples, allows for simple loading because of its low volatility, and provides a hydrostatic environment comparable to that of other known pressure media, including iso-n-pentane and methanol-ethanol mixtures.^{16,17} From literature, we note that at ~ 3 GPa, anisotropic forces begin to arise for silicone oil with viscosity of 1 Pa·s.¹⁷ For Dow Corning 200, this value is at 3.8 GPa,¹⁸ though other reports observe pressure gradients at higher values, ranging from 8.9 GPa¹⁹ to 15 GPa.²⁰ In our *in situ* XRD

experiment on 0% Mn^{2+} -doped α -NPs, we do not see significant deviation in the elastic modulus along different crystallographic axes, suggesting a hydrostatic environment throughout the entire pressure regime we probe (Figure S15b). We report a quasi-hydrostatic environment, because the data for 2.8% Mn^{2+} -doped α -NPs indicates a slightly higher modulus (i.e. “stiffer”) in the (200) direction (Figure S15d). This may be a result of inhomogenous coverage of particles in silicone oil for this particular DAC loading and/or differences in mechanical properties due to Mn^{2+} -doping. Regardless, the difference due to anisotropic strain is at most 0.1%, an order of magnitude smaller than the isotropic 1.1% compressive strain. An ongoing area of research of ours includes determining how Mn^{2+} -doped samples respond to isotropic versus anisotropic stress, using different pressure media in the DAC and atomic force microscopy.

Consistent optical readouts for all nanoparticles

In Figures S5-S11, we display our measurements for the complete α -phase and β -phase series. Panel a) for each of the figures shows UC and PL integrated intensity ($I_g + I_r$), normalized to the ambient value over two pressure cycles. As described in the main text, we exclude the g_1 peak in PL data; additionally, an inset shows a representative optical image of PL. Cycle 1 data are represented in black, while Cycle 2 data are in blue. Panel b) shows the absolute I_r/I_g values in UC and PL over two pressure cycles. For each cycle, the pressure sensitivity, $\Delta \frac{I_r}{I_g}$ (% per GPa) is reported within the graphs. The R^2 values, which tell us how well $\frac{I_r}{I_g}$ follow the linear trend, are reported in Tables S4 and S5. Panel c) shows the optical images collected at select pressure points during the two cycles for select pressures. In each of the figures, the brightness is adjusted equally across all pressures in order to maintain relative color and intensity information.

Besides key trends mentioned in the main text, other noticeable trends include 1) the monotonic decrease of intensity with pressure, which is greater for UC than PL signal, and

2) deviation of $\frac{I_r}{I_g}$ values from the linear fits at low, <0.5 GPa pressures.

Intensity

In all cases, intensity decreases with increasing pressure, indicating nonradiative losses (e.g. phonon relaxation, surface quenching, cross-relaxation). Generally, α -phase NPs exhibit up to $\sim 40\%$ (UC) or $\sim 20\%$ (PL) decrease in intensity, while β -phase NPs exhibit up to $\sim 50\%$ (UC) or $\sim 20\%$ (PL) decrease in intensity. Because UC is a multiphoton process with additional energy transfer steps, it is more susceptible to quenching and nonradiative relaxation than PL, a single-photon process (see Figure S13 for details). Hence, it is not surprising that UC-intensity is more sensitive to external pressure than the PL-intensity. Additionally, we notice some inconsistency of trends between compression cycles, especially in UC. We attribute this observation partly to the Ti:Sapphire laser power fluctuations, detailed in Figure S4. Additionally, the steel gasket sample chamber sometimes shrinks at higher pressures, despite the pre-indentation procedure (see Methods), which would reduce the area evaluated on the spectrometer CCD camera.

Color

At low <0.5 GPa pressures, there is greater spread in $\frac{I_r}{I_g}$ values, contributing to the error in our linear fits. Pressure points <0.1 GPa are at the resolution limit of the DAC and pressure calibration (± 0.05 GPa or about ± 100 nN). However, our measurements suggest that those above are real optical effects. In UC data of α -4.8% (Figure S8b), for example, there is a consistent decrease of I_r/I_g within 0.5 GPa, before the positive linear trend dominates at higher pressures. Additionally, UC data in both β -0% (Figure S9b) and β -0.5% (Figure S10b) show an initial decrease of I_r/I_g , though we cannot definitively confirm consistency between cycles due to the larger initial loading pressures. Nevertheless, these results show the potential of these upconverters for sensing below the nano-Newton force range. Future studies using atomic force microscopy (AFM) will provide pico-Newton resolution and even

allow for single-particle characterization.

Pressure sensitivity values

Tables S6-S9 summarize the pressure sensitivity values in UC and PL for both crystal phases. Typically, steeper slopes from linear fits of the $\frac{I_r}{I_g}$ data indicate greater color responses to applied pressure. However, as explored in the main text, the initial control or ambient values, $\frac{I_{ro}}{I_{go}}$, to which relative changes are compared, can vary significantly due to crystal phase (higher for α -NaYF₄), type of luminescence (higher in UC), and *d*-metal doping concentrations (higher with increasing Mn²⁺). In Figure 2, the control samples with 0% Mn²⁺-doping, for instance, have $\frac{I_{ro}}{I_{go}}$ values of 10.85 (α -UC), 0.42 (α -PL), 1.06 (β -UC), and 0.12 (β -PL), which increase with higher Mn²⁺-doping. The measured and fitted ratio at ambient pressure, $\frac{I_{ro}}{I_{go}}$, for each type of nanoparticle loaded in the DAC is also listed in these tables and follow similar trends to the dropcasted film studies. Observed differences in values of the DAC versus film studies may result from changes in illumination intensity (i.e. power loss through the diamond culet) or changes in the NPs induced by pressing (i.e. DAC ambient values are often from the release portion of the first cycle). Additionally, for PL in the DAC, the definition of $\frac{I_{ro}}{I_{go}}$ excludes the g_1 peak.

Therefore, we also report the absolute pressure sensitivity, defined as $\Delta_{abs} \frac{I_r}{I_g}$ per GPa. Here,

$$\Delta_{abs} \frac{I_r}{I_g} = \frac{I_r}{I_g} - \frac{I_{ro}}{I_{go}} \quad (4)$$

In a similar fashion described in the Methods, we linearly fit $\Delta_{abs} \frac{I_r}{I_g}$ with respect to pressure and extract the slope (i.e. absolute pressure sensitivity). The absolute pressure sensitivity is therefore related to the relative pressure sensitivity by a factor of $\frac{I_{ro}}{I_{go}}$ (see Equation (2) for comparison; quantities are also listed in Tables S6-S9). While this factor does not alter the key trends for pressure sensitivity (see Figure S12), and in fact, makes the α -UC series even more sensitive relative to the others (note the break in the y-axis scale), it does alter the scale

for each type of NP according to its initial spectral shape. This means that UC-sensitivities will be at least an order of magnitude higher than PL-sensitivities.

Analysis of energetic interactions

In Figure S13, we present a simplified energy level diagram of our system, detailing both the multiphoton process for UC and single photon process for PL. Because lanthanide f-f transitions are Laporte forbidden,²¹ they are long-lived and allow for multiple NIR photons to excite the system and produce radiative emission in visible frequencies. In UC, the commonly accepted mechanism by which the green states g_1 ($^2H_{11/2}$) and g_2 ($^4S_{3/2}$) are populated is through two-photon excitation, with energy transfer between Yb^{3+} and Er^{3+} . While this process also contributes to population of the red state ($^4F_{9/2}$), as in the case for PL, it has more recently been discovered that a three-photon process can also populate the red state.^{22,23} In this process, an additional NIR photon is absorbed to reach the $^4G, ^2K$ manifolds, which then, through multiphonon relaxation and back transfer, decays into $^4F_{9/2}$. In PL, under 488 nm illumination, $^4F_{9/2}$ is directly excited, yielding fundamentally different energetic pathways compared to UC.

Given the crystal field sensitivity of d -metals, we expect that the position of the 4T_1 Mn^{2+} energy level is highly dependent on the symmetry environment of the Mn^{2+} ion within the $NaYF_4$ host (Figure 1a). Ongoing research is currently under way to directly probe the $^4T_1 \rightarrow ^6A_1$ Mn^{2+} transition in the two crystal phases, though we reference recent literature in creating our energy level diagram (i.e. 535 nm for α - $NaGdF_4$ ⁹ or 561 nm for Gd^{3+} , Mn^{2+} co-doped α - $NaYF_4$ ²⁴). In both cases, the energy level approximately coincides with the radiative Er^{3+} green states, allowing for coupling between Mn^{2+} and Er^{3+} emission. Here, coupling is defined as how well the Mn^{2+} ion transfers energy from Er^{3+} green to red. As observed in the pre-stress studies (Figure 2), coupling is weak in α - $NaYF_4$ and strong in β - $NaYF_4$. Besides intrinsic $\frac{I_r}{I_g}$ and doping-induced strain, the position of the Mn^{2+} energy level

in relation to the green states (i.e. spectral overlap) would also impact coupling strength.

With pressure, a combination and competition of effects alter coupling and emission properties; these effects include shifting energy levels, decreasing interionic distances, spectral broadening, surface quenching, and more. As schematically represented in Figure S13a and S13b, based on our observations from DAC pressure measurements, we hypothesize that the coupling is enhanced in α -NaYF₄ and decreased in β -NaYF₄ with pressure. We believe that a shift in the Mn²⁺ energy level would be the largest contributor to the observed optical responses. In a previous pressure-dependent study on Mn²⁺-doped ZnS, for example, the Mn²⁺ phosphorescence red-shifts nearly 30 nm with similar 3.5 GPa pressures.²⁵ In this study, it is likely that both the position of the ambient Mn²⁺ energy level and the magnitude of the pressure-induced shift differs in the α -NaYF₄ versus β -NaYF₄ lattice, resulting in our observations that α -NaYF₄ NPs get “redder” with pressure and optimized β -NaYF₄ NPs gets “greener” with pressure. Hence, beyond applications for force-sensing, these NPs present a rich system for further investigation of energetics between lanthanides and *d*-metals.

Decrease in pressure sensitivity for α -1.7%

In Figure 4a of the main text, there is an initial decrease of pressure sensitivity for α -NaYF₄ with 1.7% Mn²⁺ before enhancement at higher doping concentrations. We can reconcile this by looking at the pre-stress, optical and structural effects of Mn²⁺-doping. In particular from Figure 2b, the introduction of Mn²⁺-doping decreases $\frac{I_r}{I_g}$ in UC, suggesting that crystal defects, including F⁻ vacancy centers⁹ and lattice strain (Figure S2c), might hinder the energetic coupling between Er³⁺ and Mn²⁺ through nonradiative or quenching pathways. From corresponding PL data in Figure 2b, we confirm that the coupling is viable, provided that relevant Er³⁺ and Mn²⁺ energy levels are effectively populated (Figure S13a). Thus, while applying pressure may improve coupling, there appears to be a doping barrier before sensitivity, as defined in our study, is enhanced compared to the undoped control case. As doping concentration is increased beyond 1.7% in Figure 2b, the pre-stress $\frac{I_r}{I_g}$ in UC is

recovered. Meanwhile, increasing Mn^{2+} doping does not increase lattice strain significantly (Figure S2c). The combination of these effects support better energetic coupling, and as a result, improve pressure sensitivity.

Structural robustness and mechanical properties

After two cycles of compression and release, we collect post-DAC NPs by removing the steel gasket and sonicating it in cyclohexane. The solution is then dropcasted on an ultra-thin carbon grid for TEM imaging. Generally, the NPs maintain their size and morphology, as seen in Figure S14. We attribute the clumping to difficulty in dispersing the silicone-oil-immersed NPs in cyclohexane.

Additionally, we perform pressure-dependent *in situ* XRD on α -phase NPs at Sector 16 of Argonne National Laboratory’s Advanced Photon Source (APS). DACs were loaded as before (Methods) and illuminated with an X-ray source of 0.3738 Å. The pressure from ruby PL is measured before and after obtaining each 2D Debye-Scherrer diffraction image. We report the average of the two pressures and convert the 2D rings into 1D patterns using FIT2D software. Figure S15a and S15c show the XRD patterns for α -0.0% and α -2.8%, respectively, in which no phase-change is detected. For each of the four lowest-order reflections, we find peak positions using Gaussian fits and calculate the change in lattice parameter, or strain. The linear stress-strain behavior during compression indicates that we are probing the elastic regime of the nanoparticles, though there appears to be some hysteresis upon release. This is consistent with previous literature that shows plastic deformation or yield stress at around 10 GPa.⁸ From the linear fits in Figure S15b and S15d, we derive the elastic moduli along particular crystallographic axes. For 0% Mn^{2+} -doped particles, the elastic moduli are consistent for all reflections, with an average elastic modulus of 272 ± 2 GPa. Meanwhile, the 2.8% Mn^{2+} -doped case shows slight anisotropy (up to 300 GPa for the (200) reflection), with an average elastic modulus of 286 ± 5 GPa. In both cases, the maximum

lattice strain is about -1.1%. Thus, the average length of one cubic NP decreases by ~ 0.2 nm at the highest pressure we probe.

Cyclability

We perform up to five cycles for a Mn^{2+} -doped $\alpha\text{-NaYF}_4$ sample, displayed in Figure S16. Here, the measured $\frac{I_{ro}}{I_{go}}$ is 12.25 ± 0.03 in UC and 0.929 ± 0.008 in PL, while the fitted $\frac{I_{ro}}{I_{go}}$ is 12.44 ± 0.14 in UC and 0.935 ± 0.006 in PL. Since we probe the elastic regime (Figure S15), we do not expect sensitivities to decrease significantly. In fact, this experiment shows that the average slope or pressure sensitivity improved with more cycles. These fitted sensitivities are lower than those reported in the main text, probably as a result of fewer data points in the low, <0.5 GPa pressure regime, where there is more scatter. In Figure 4b, for example, there seems to be an initial decrease in the ratio within 0.5 GPa for both Cycle 1 and Cycle 2, before the positive linear trend dominates at higher pressure. 3 of 48 UC spectra collected at the 16 pressure points showed systematic errors (e.g. laser quality) and were therefore excluded from the figure and analysis.

Dynamic range and resolution of optical sensors with respect to force

Per calculations described in the Methods section, we convert pressures into the total magnitude of force exerted on each nanoparticle. Surface areas are calculated using the morphology and statistical analysis of TEM images (Figure S1), as well as their pressure dependence from *in situ* XRD data (Figure S15). Conversions are graphically represented in Figure S17; note that the errors arise predominately from the dispersion of nanoparticle size. Hence, the $\beta\text{-NaYF}_4$ nanoparticles have better force resolution (conservatively, ~ 1 μN) over the pressure range we probe. Better force quantification can be achieved through future, single-particle

calibrations using atomic force microscopy. Meanwhile, the dynamic range is at least 0.05 GPa (resolution of DAC and ruby PL) to 3.5 GPa pressures, which corresponds roughly to 100 nN to 10 μ N forces. In this study, we are primarily limited by the inability to exert finer increments of pressure with the diamond anvil cell. With AFM, we can probe smaller, pico- to nano-Newton forces. In terms of the upper force limit, we expect that to occur when the nanoparticles plastically deform, at around 10 GPa.⁸ For these higher pressures, another pressure medium may be needed to maintain a hydrostatic or controlled environment within the DAC.

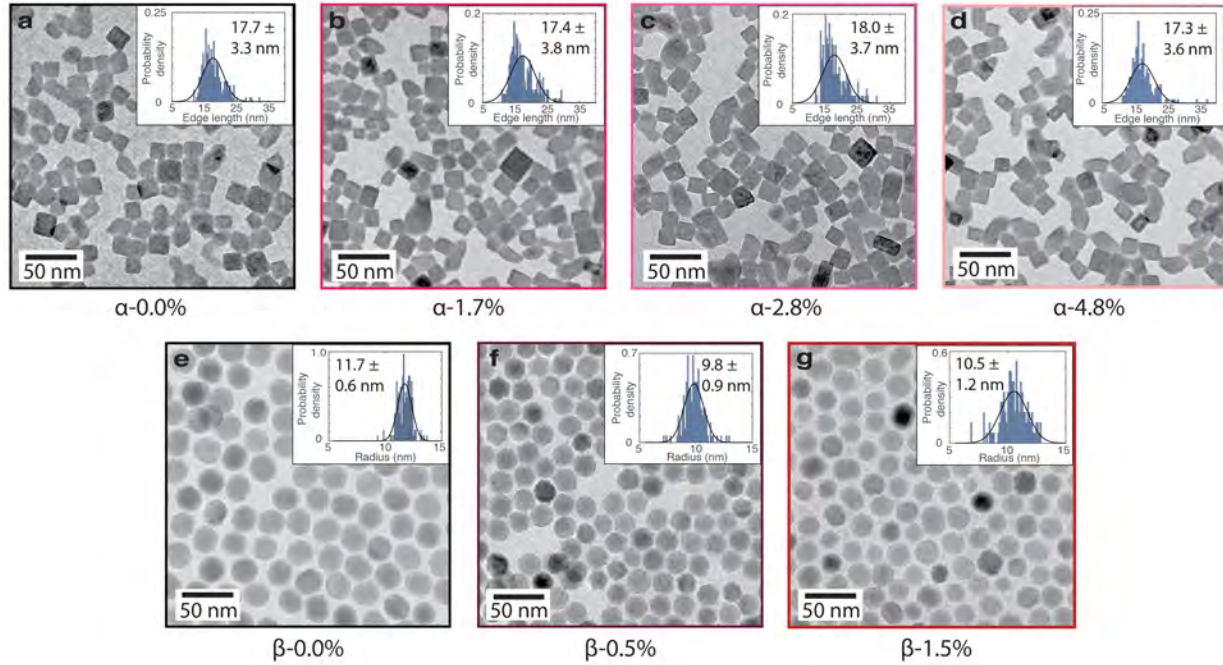


Figure S1: Size, morphology, and uniformity of nanoparticles

TEM images of nanoparticles in the a-d) α -series and e-g) β -series. The insets are histograms of 150-300 nanoparticles: edge length of cubic α -NPs or radius of spherical β -NPs. For each histogram, a Gaussian probability density function curve is fitted to extract the mean size and standard deviation of the NPs.

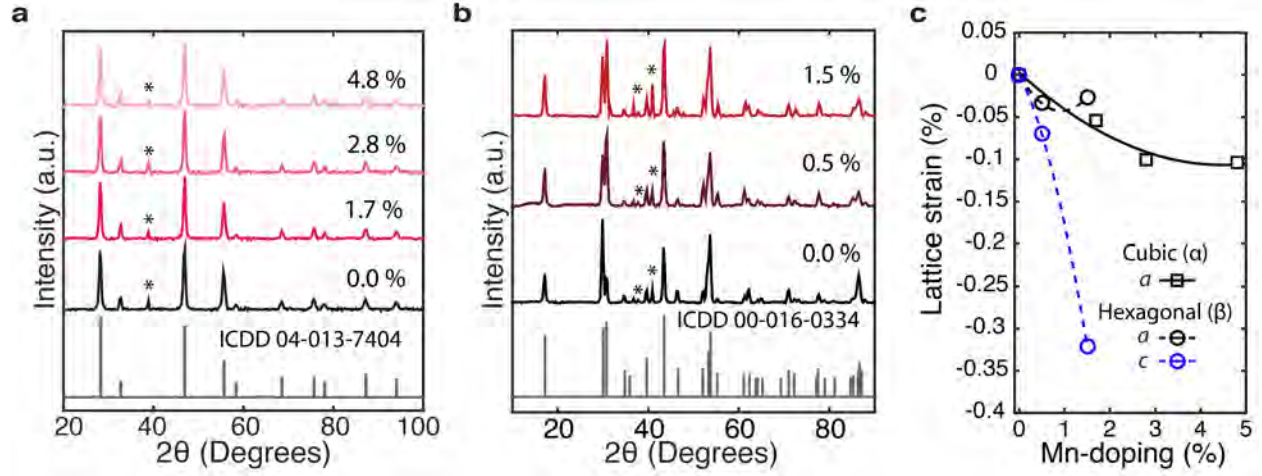


Figure S2: Crystal lattice and phase characterization

XRD patterns acquired using Cu $K\alpha_1$ X-rays ($\lambda = 1.54056 \text{ \AA}$) for a) α -phase and b) β -phase nanoparticles. Samples at various doping concentrations are consistent with the ICDD standard pattern 04-013-7404 (α -NaYF₄) and 00-016-0334 (β -NaYF₄). c) Lattice strain for α -phase constant a (solid guide-to-the-eye) and β -phase constants a and c (dashed guides-to-the-eye) are extracted from Pawley fitting experimental diffraction peaks. Peaks marked by an asterisk are attributed to NaF (39°) and the aluminum sample holder (38° and 41°).

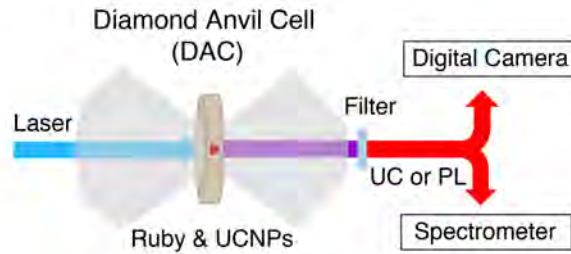


Figure S3: Experimental DAC schematic

A symmetric DAC is coupled to both a 980 nm and 488 nm laser source. NPs and a bulk ruby for pressure calibration are loaded in between two diamond culets. A filter eliminates signal from the laser source and the resulting UC or PL emission is recorded by a digital camera and spectrometer.

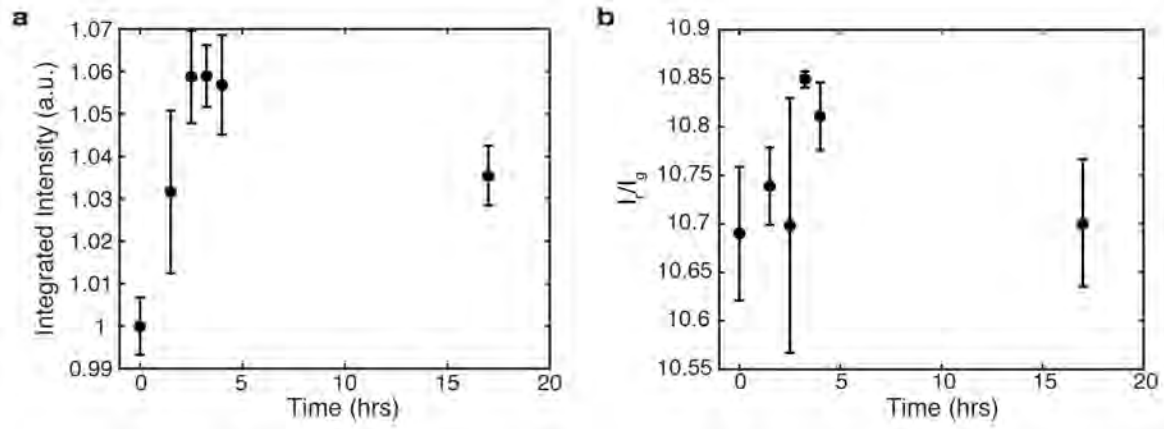


Figure S4: Time dependence of optical readouts in UC

a) Integrated intensity over all emission peaks, $I_r + I_g$, and b) $\frac{I_r}{I_g}$ values recorded over 17 hours at a constant pressure, following typical DAC spectra collection procedures (see Methods). Error bars indicate the standard deviation of values derived from three spectra collected at each time point.

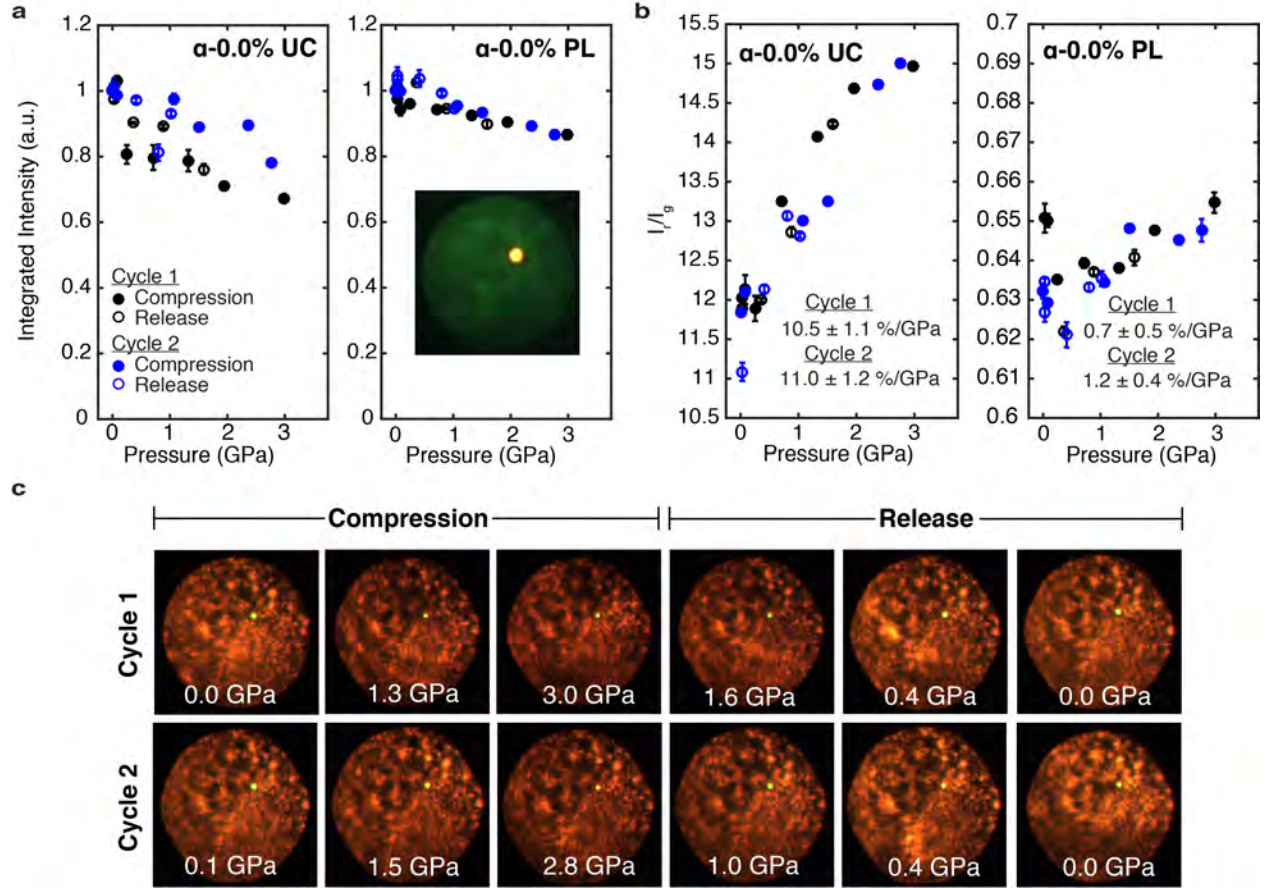


Figure S5: Optical force-response for 0.0% Mn^{2+} -doped α - NaYF_4 nanoparticles
 For two pressure cycles, we collect UC and PL spectra and track the a) integrated intensity, $I_r + I_g$, and b) red to green ratio, I_r/I_g . The color pressure sensitivity values for Cycle 1 (black) and Cycle 2 (blue) are also listed. c) Corresponding optical images in UC show intensity and color responses for select pressures. A representative PL image is also displayed.

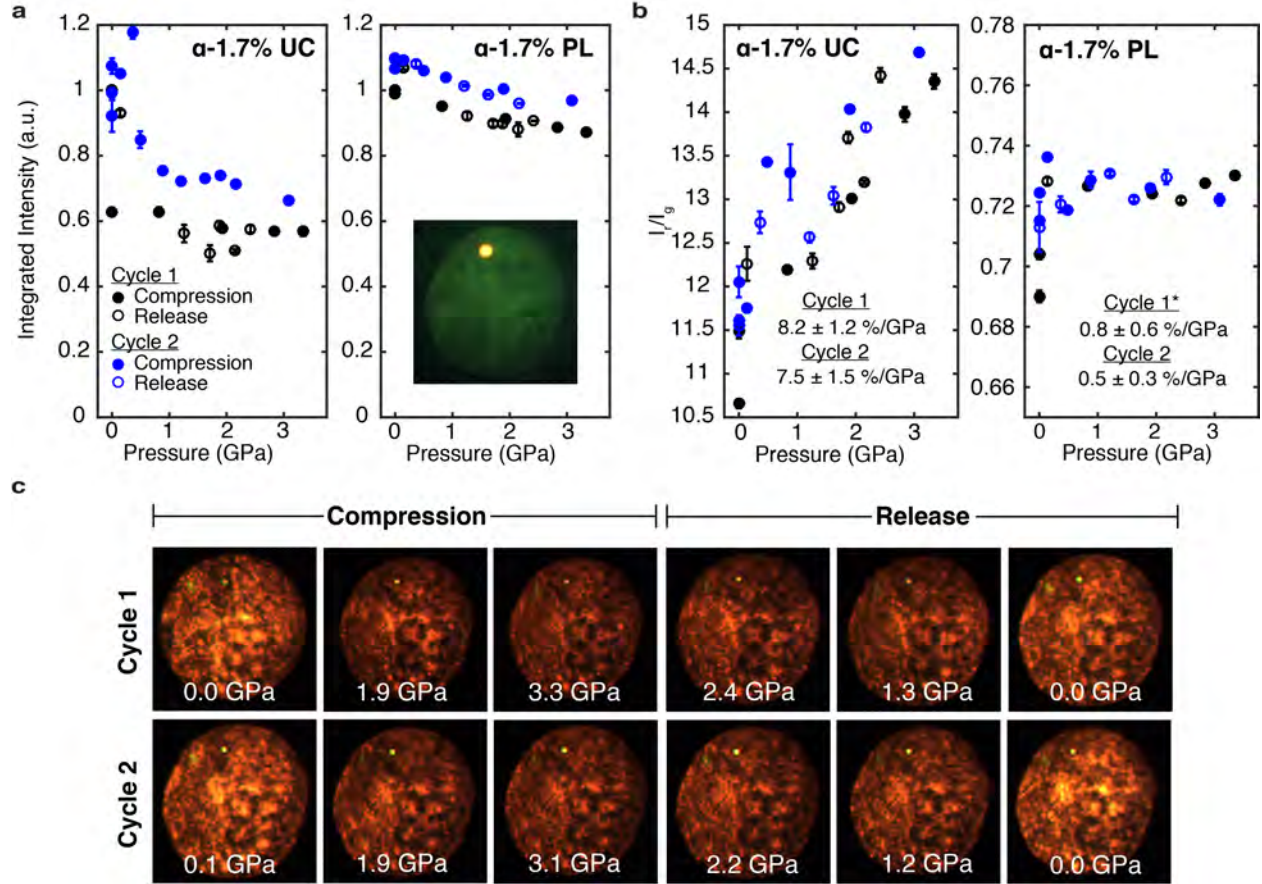


Figure S6: Optical force-response for 1.7% Mn^{2+} -doped α - NaYF_4 nanoparticles For two pressure cycles, we collect UC and PL spectra and track the a) integrated intensity, $I_r + I_g$, and b) red to green ratio, $\frac{I_r}{I_g}$. The color pressure sensitivity values for Cycle 1 (black) and Cycle 2 (blue) are also listed. c) Corresponding optical images in UC show intensity and color responses for select pressures. A representative PL image is also displayed.*In the main text, the PL pressure sensitivity for the second cycle is reported due to outliers in the first cycle during release (not shown above or included in the fitting).

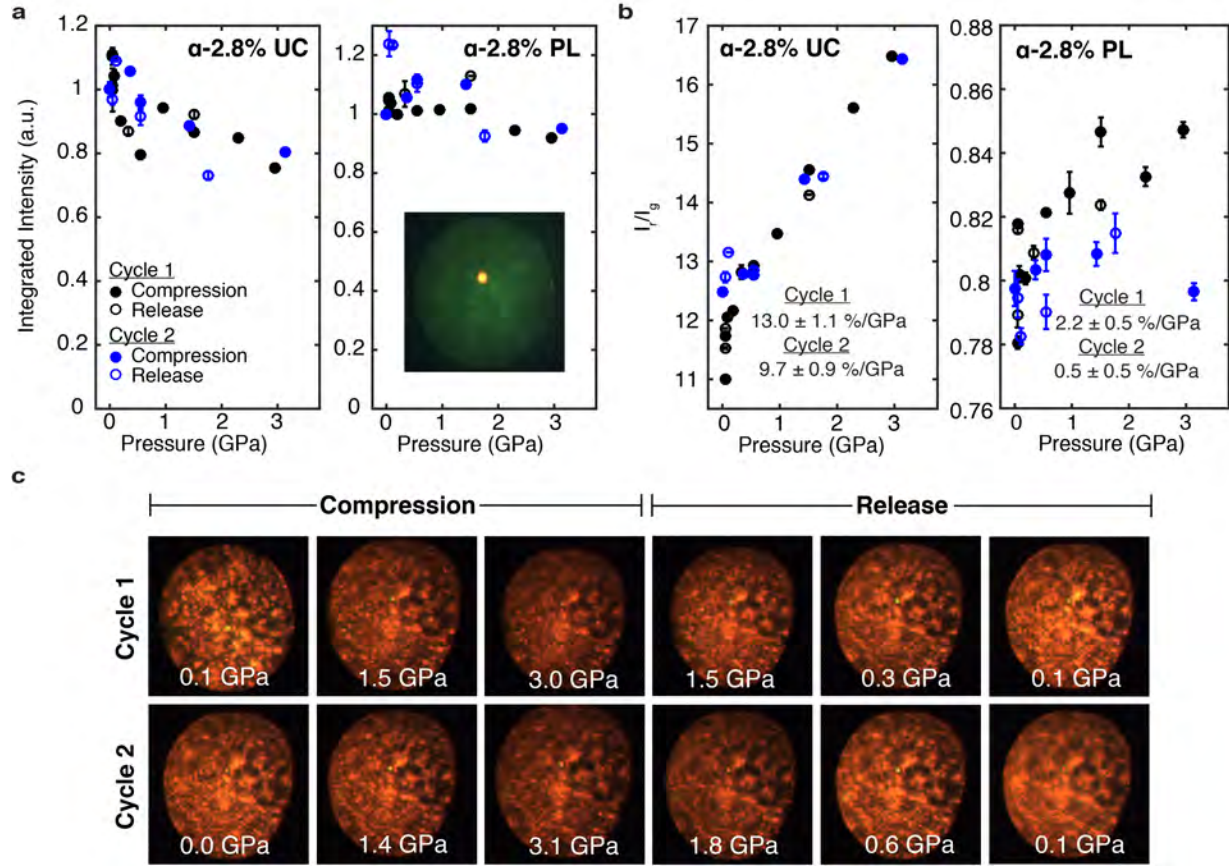


Figure S7: Optical force-response for 2.8% Mn^{2+} -doped $\alpha\text{-NaYF}_4$ nanoparticles For two pressure cycles, we collect UC and PL spectra and track the a) integrated intensity, $I_r + I_g$, and b) red to green ratio, $\frac{I_r}{I_g}$. The color pressure sensitivity values for Cycle 1 (black) and Cycle 2 (blue) are also listed. c) Corresponding optical images in UC show intensity and color responses for select pressures. A representative PL image is also displayed.

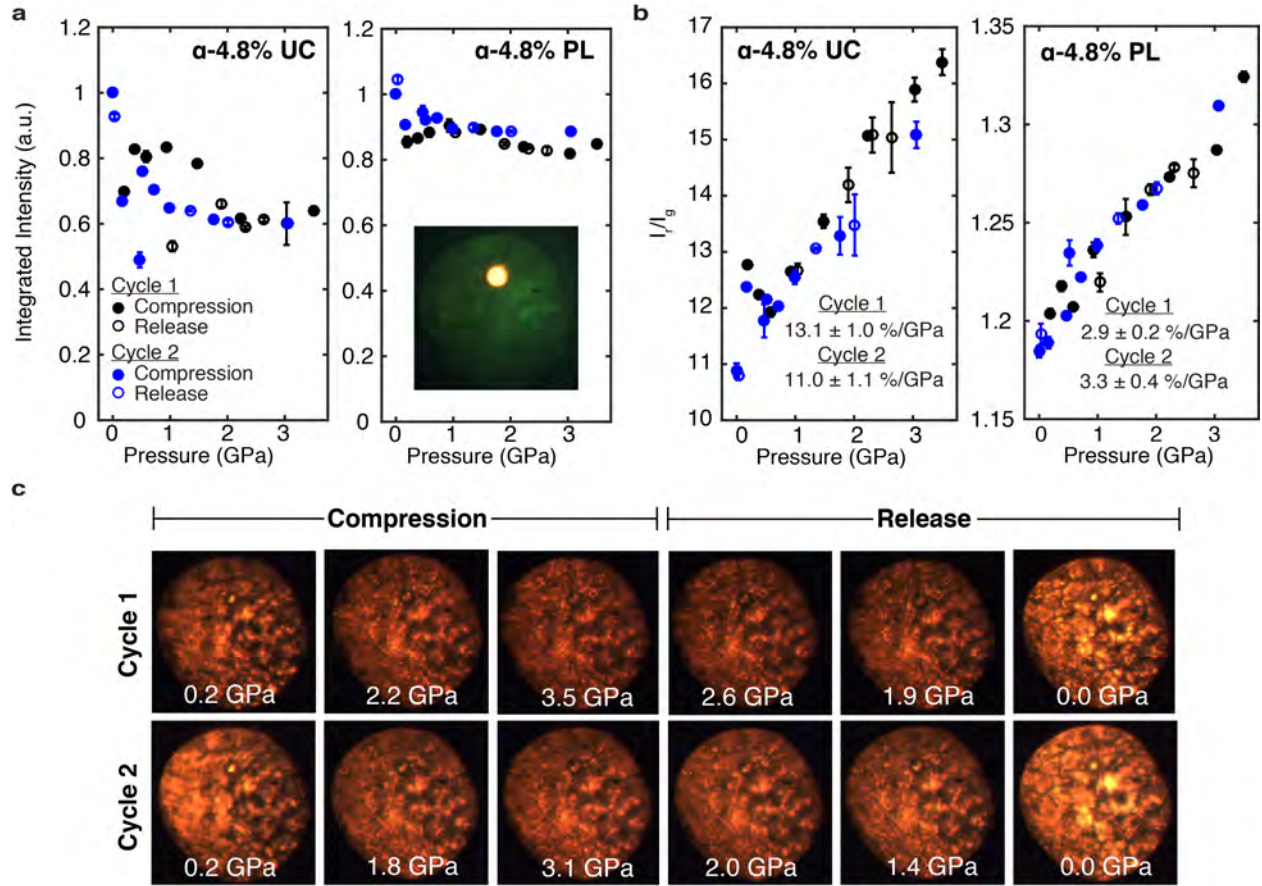


Figure S8: Optical force-response for 4.8% Mn^{2+} -doped $\alpha\text{-NaYF}_4$ nanoparticles For two pressure cycles, we collect UC and PL spectra and track the a) integrated intensity, $I_r + I_g$, and b) red to green ratio, $\frac{I_r}{I_g}$. The color pressure sensitivity values for Cycle 1 (black) and Cycle 2 (blue) are also listed. c) Corresponding optical images in UC show intensity and color responses for select pressures. A representative PL image is also displayed.

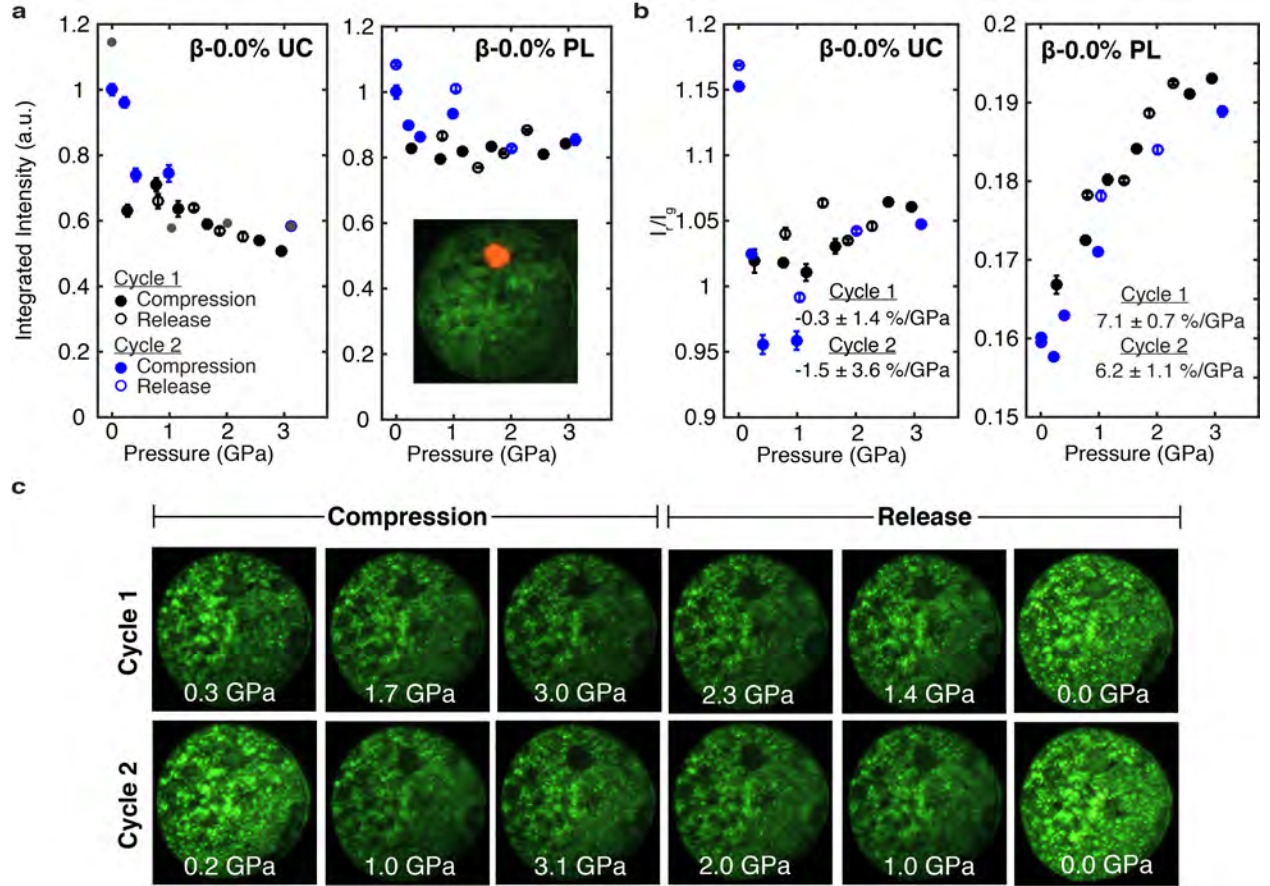


Figure S9: Optical force-response for 0.0% Mn^{2+} -doped $\beta\text{-NaYF}_4$ nanoparticles For two pressure cycles, we collect UC and PL spectra and track the a) integrated intensity, $I_r + I_g$, and b) red to green ratio, $\frac{I_r}{I_g}$. The color pressure sensitivity values for Cycle 1 (black) and Cycle 2 (blue) are also listed. c) Corresponding optical images in UC show intensity and color responses for select pressures. A representative PL image is also displayed.

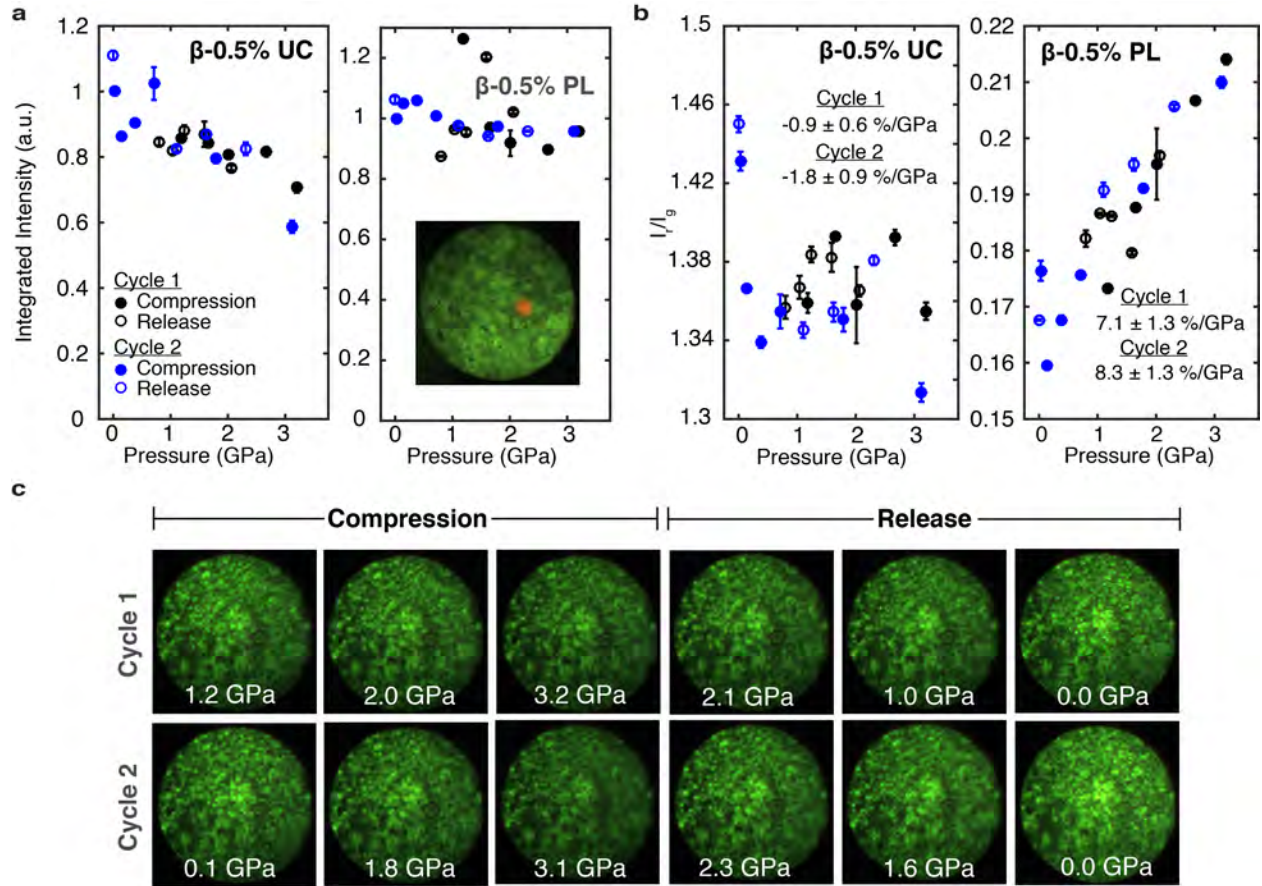


Figure S10: Optical force-response for 0.5% Mn^{2+} -doped β - NaYF_4 nanoparticles For two pressure cycles, we collect UC and PL spectra and track the a) integrated intensity, $I_r + I_g$, and b) red to green ratio, $\frac{I_r}{I_g}$. The color pressure sensitivity values for Cycle 1 (black) and Cycle 2 (blue) are also listed. c) Corresponding optical images in UC show intensity and color responses for select pressures. A representative PL image is also displayed.

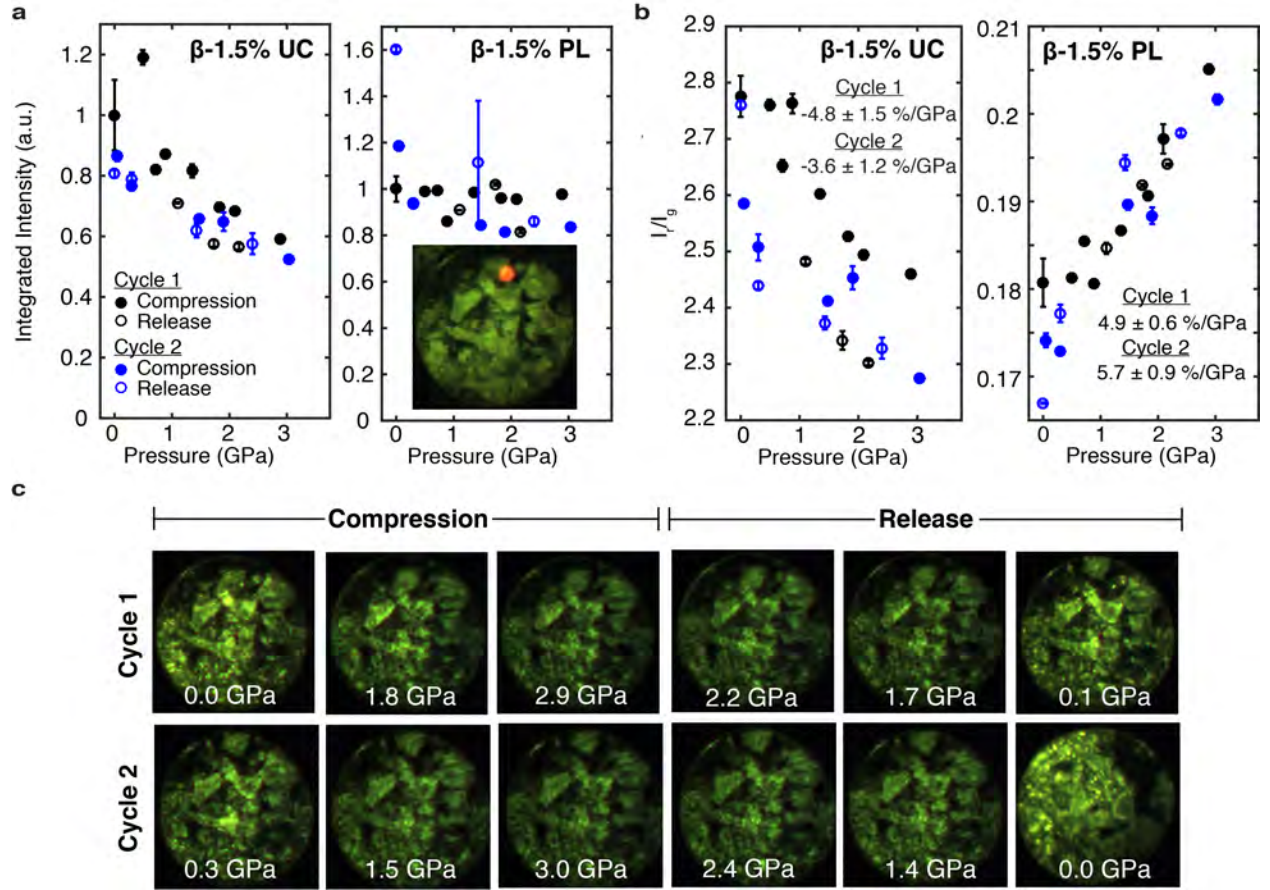


Figure S11: Optical force-response for 1.5% Mn^{2+} -doped $\beta\text{-NaYF}_4$ nanoparticles For two pressure cycles, we collect UC and PL spectra and track the a) integrated intensity, $I_r + I_g$, and b) red to green ratio, $\frac{I_r}{I_g}$. The color pressure sensitivity values for Cycle 1 (black) and Cycle 2 (blue) are also listed. c) Corresponding optical images in UC show intensity and color responses for select pressures. A representative PL image is also displayed.

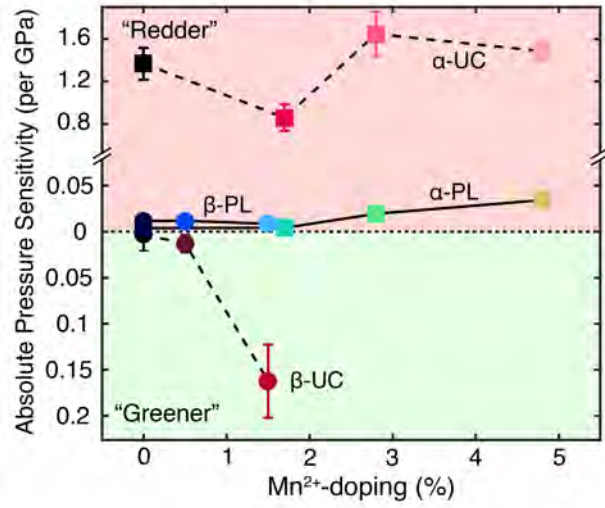


Figure S12: Absolute pressure sensitivity of optical sensors a) Absolute change in the red to green ratio, $\Delta_{abs} \frac{I_r}{I_g}$, due to one GPa of applied pressure. Similar to Figure 4 of the main text, points in the red (green)-shaded region indicate NPs that become “redder” (“greener”) with pressure. Error bars represent half of the 95% confidence interval of fitted slopes for $\frac{I_r}{I_g}$ with pressure.

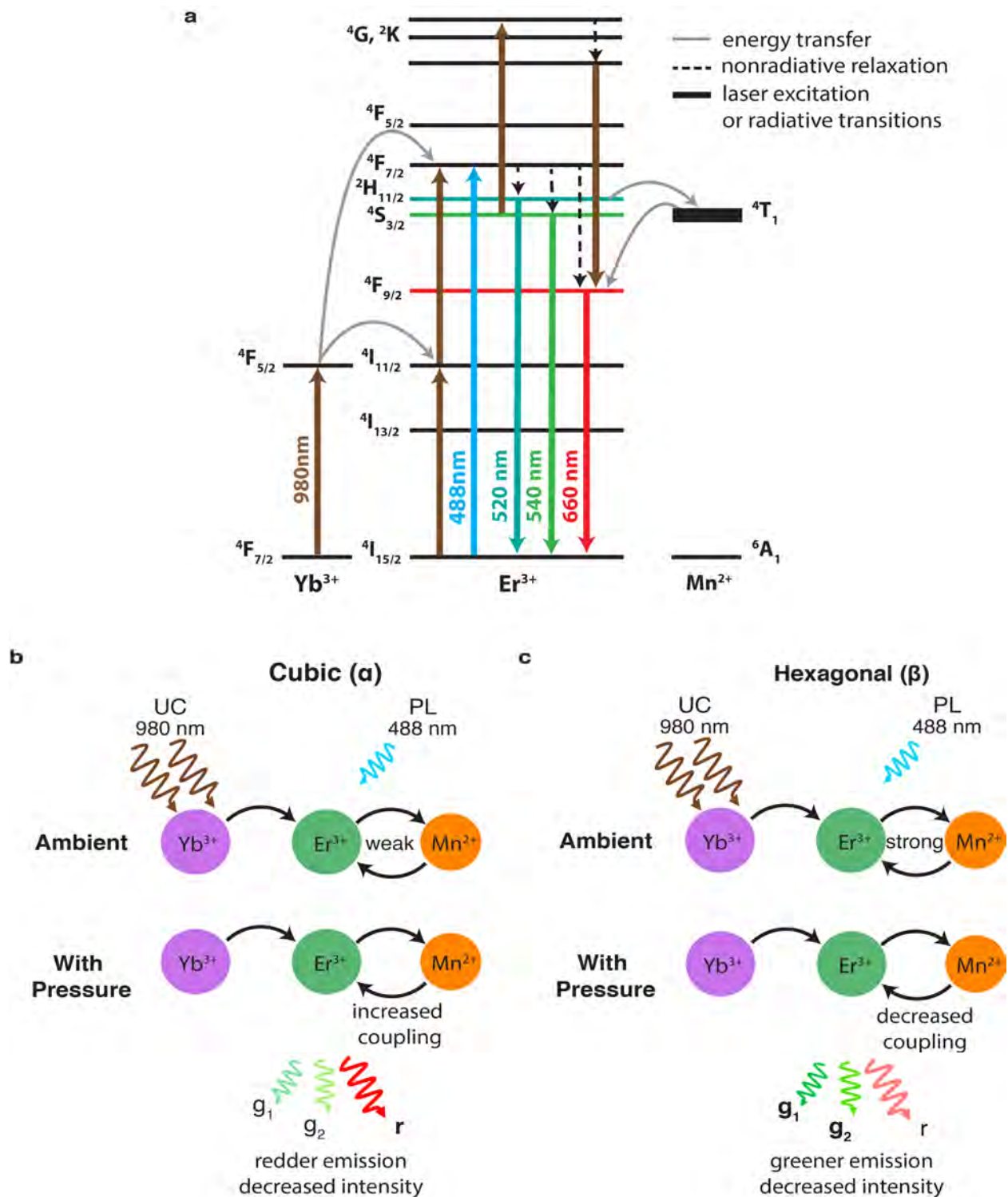


Figure S13: Energetics underlying UC and PL with and without pressure
a) Energy level diagram detailing the multiphoton and single photon process for UC and PL through the Yb^{3+} , Er^{3+} , and Mn^{2+} system. Schematic representation of spectral changes for b) cubic (α) and c) hexagonal (β) NPs, as observed in our experiments.

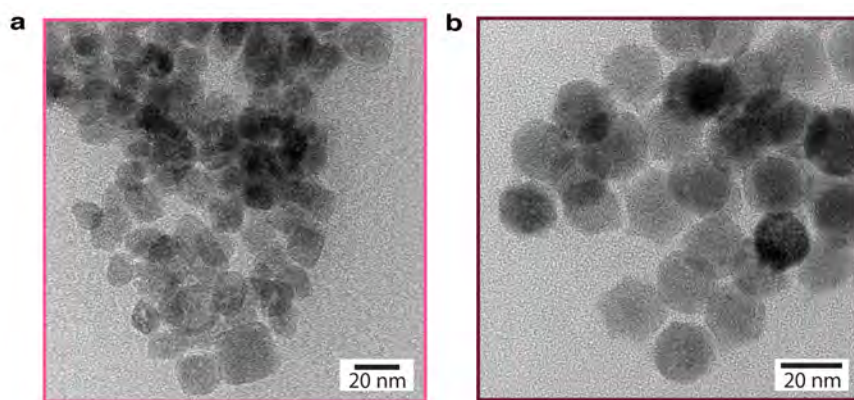


Figure S14: Post-DAC morphology of nanoparticles

TEM images of representative a) α -phase and b) β -phase nanoparticles collected from the DAC after two consecutive pressure cycles

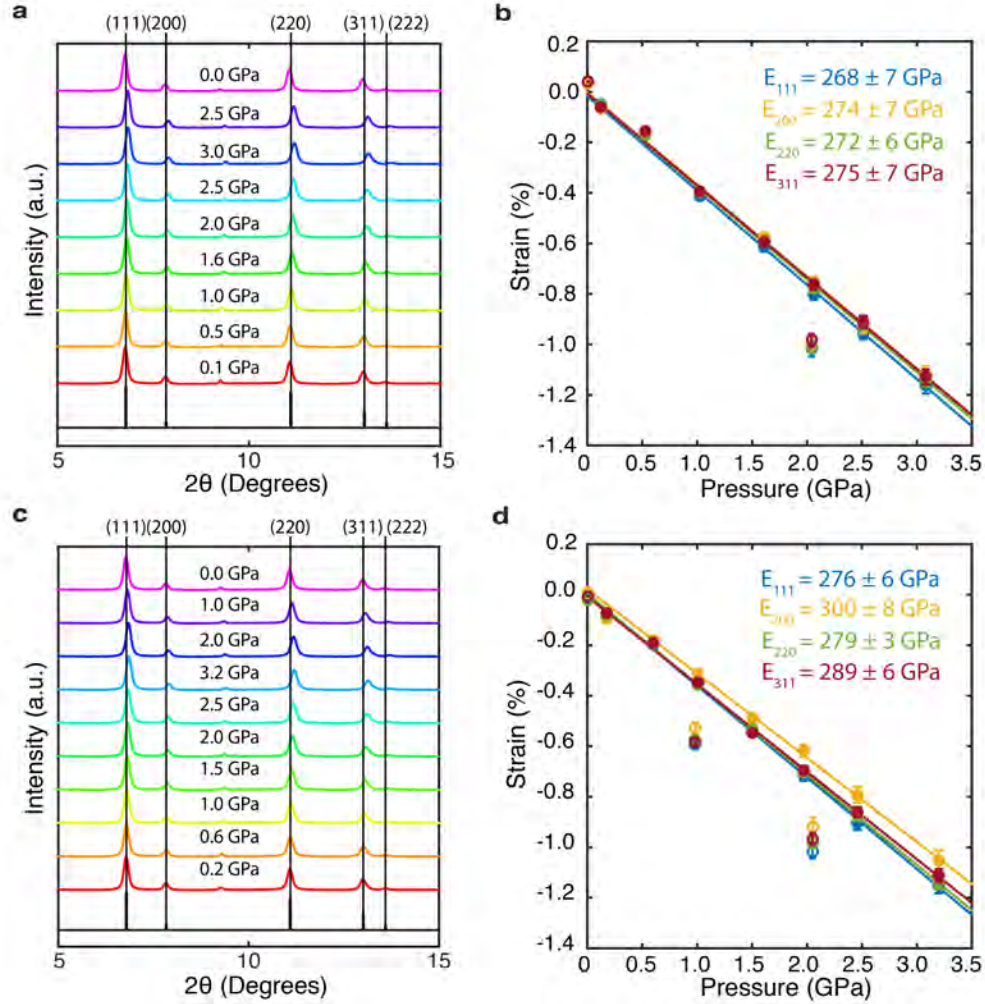


Figure S15: Crystal structure during one pressure cycle

Diffraction patterns for a) 0% and c) 2.8% Mn²⁺-doped α -phase NPs at increasing (red to blue) and decreasing (blue to pink) pressures. Pressure-dependence of the lattice parameter derived from different diffraction peaks for b) 0% and d) 2.8% Mn²⁺-doped α -phase NPs.

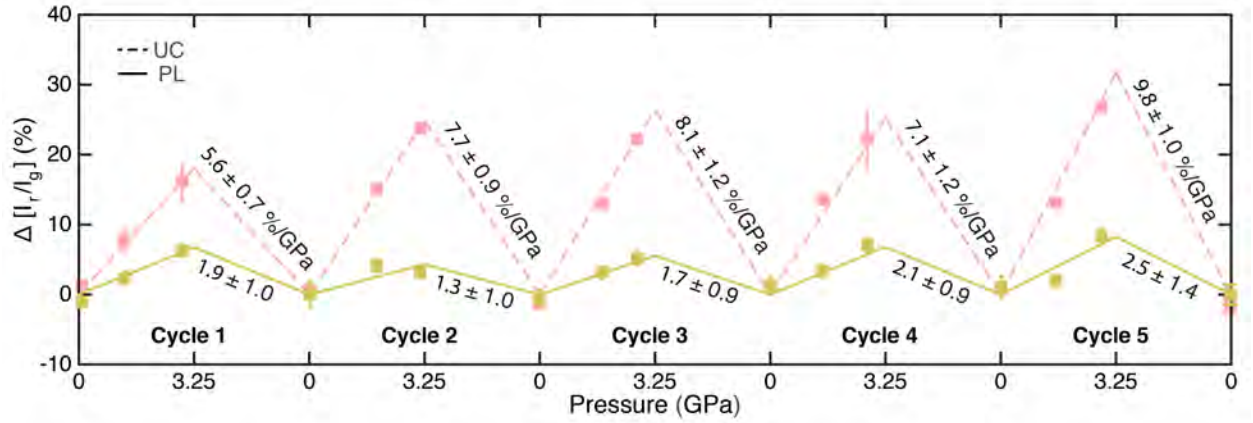


Figure S16: Cycling of 4.9 % Mn²⁺-doped α -NaYF₄

DAC pressure measurements for 5 cycles of compression and release on the Mn²⁺-doped α -NPs in UC (dashed) and PL (solid). Error-weighted linear fits are determined for each cycle using both compression and release data points. Pressure sensitivity values or the percent change in the red to green ratio, $\Delta \frac{I_r}{I_g}$ (%), due to one GPa of applied pressure are listed for each cycle.

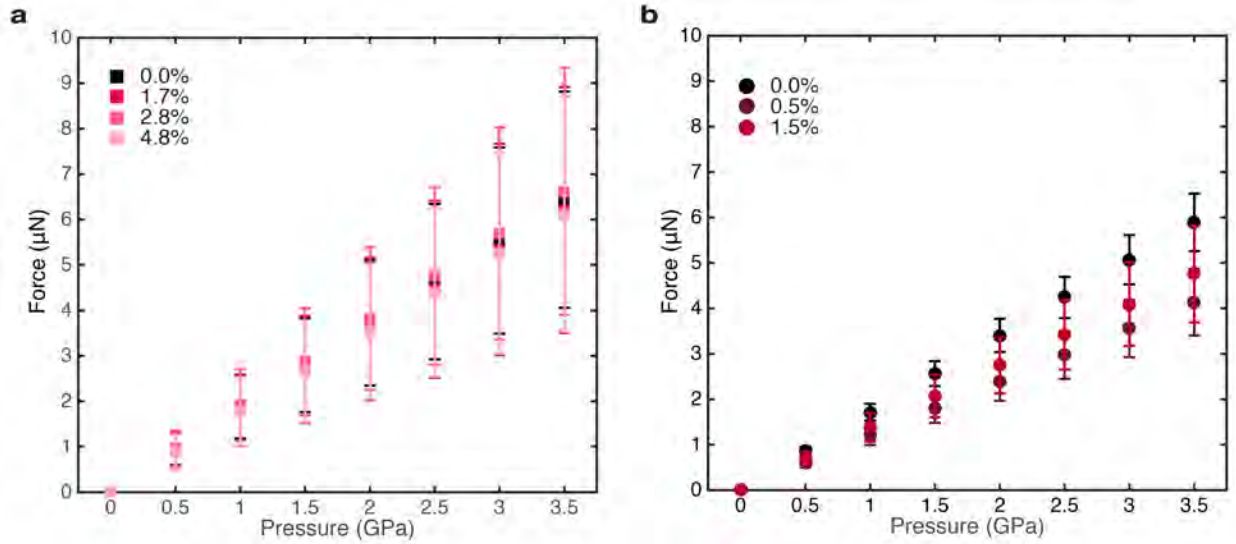


Figure S17: Pressure to force conversion

Per calculations described in the Methods section, we convert pressures into the total magnitude of force exerted on each nanoparticle in the a) α -series and b) β -series. Surface areas are calculated using the morphology and statistical analysis of TEM images (Figure S1), as well as their pressure dependence from *in situ* XRD data (Figure S15). Here, the larger uncertainty of force in the α -series comes from higher dispersion in particle size.

Table S1: Elemental analysis for α -NaYF₄ nanoparticles

As synthesized Mn (%)	# of samples	Mn (%)	Y (%)	Yb (%)	Er (%)	Yb/Er
0	6	0.0 \pm 0.0	79.5 \pm 0.4	18.6 \pm 0.4	1.9 \pm 0.1	9.7 \pm 0.3
3	3	1.7 \pm 0.2	77.4 \pm 2.3	18.8 \pm 2.0	2.1 \pm 0.1	8.9 \pm 0.5
5	6	2.7 \pm 0.3	74.3 \pm 0.2	21.0 \pm 0.2	2.0 \pm 0.0	10.5 \pm 0.1
10	5	4.8 \pm 0.5	72.6 \pm 1.1	20.7 \pm 0.9	2.0 \pm 0.1	10.5 \pm 1.1

Table S2: Elemental analysis for β -NaYF₄ phase nanoparticles

As synthesized Mn (%)	Mn (%)	Y (%)	Yb (%)	Er (%)	Yb/Er
0	0.0	80.0	18.1	1.9	9.3
0*	0.0	81.1	17.0	1.9	8.7
10	0.2	81.8	16.1	1.9	8.4
20*	0.5	76.0	21.2	2.2	9.5
20	0.8	77.1	19.8	2.2	9.2
30	1.3	73.3	22.6	2.7	8.6
30	2.1	73.1	22.3	2.6	8.3
40*	1.5	68.9	26.7	2.9	9.3

Table S3: Lattice constants from Pawley fits of XRD diffraction patterns

Phase	Mn (%)	<i>a</i> (Å)	<i>c</i> (Å)
α	0.0	5.47704	
α	1.7	5.47406	
α	2.8	5.47151	
α	4.8	5.47133	
β	0.0	5.97485	3.51033
β	0.5	5.97283	3.50787
β	1.5	5.97326	3.49905

Table S4: R^2 values of linear fits for α -NaYF₄ nanoparticles

Mn (%)	Cycle 1 UC R^2	Cycle 2 UC R^2	Cycle 1 PL R^2	Cycle 2 PL R^2
0.0	0.91	0.93	0.20	0.65
1.7	0.84	0.75	0.31	0.28
2.8	0.94	0.96	0.67	0.14
4.8	0.95	0.94	0.94	0.92

Table S5: R^2 values of linear fits for β -NaYF₄ nanoparticles

Mn (%)	Cycle 1 UC R^2	Cycle 2 UC R^2	Cycle 1 PL R^2	Cycle 2 PL R^2
0.0	0.0067	0.040	0.94	0.88
0.5	0.22	0.41	0.82	0.88
1.5	0.56	0.64	0.91	0.88

Table S6: UC sensitivity for α -NaYF₄ nanoparticles

Mn (%)	Measured $\frac{I_{ro}}{I_{go}}$	Fitted $\frac{I_{ro}}{I_{go}}$	Pressure sensitivity (% per GPa)	Absolute Pressure Sensitivity (per GPa)
0.0	11.85 ± 0.04	11.83 ± 0.12	10.5 ± 1.1	1.37 ± 0.15
1.7	10.66 ± 0.05	11.68 ± 0.22	8.2 ± 1.2	0.86 ± 0.12
2.8	12.48 ± 0.05	11.88 ± 0.19	13.0 ± 1.1	1.65 ± 0.21
4.8	10.89 ± 0.13	11.30 ± 0.23	13.1 ± 1.0	1.49 ± 0.10

Table S7: PL sensitivity for α -NaYF₄ nanoparticles

Mn (%)	Measured $\frac{I_{ro}}{I_{go}}$	Fitted $\frac{I_{ro}}{I_{go}}$	Pressure sensitivity (% per GPa)	Absolute Pressure Sensitivity (per GPa)
0.0	0.632 ± 0.002	0.639 ± 0.004	0.7 ± 0.5	0.004 ± 0.003
1.7	0.725 ± 0.001	0.717 ± 0.002	0.5 ± 0.3	0.004 ± 0.002
2.8	0.798 ± 0.006	0.800 ± 0.005	2.2 ± 0.5	0.019 ± 0.004
4.8	1.184 ± 0.003	1.195 ± 0.005	2.9 ± 0.2	0.034 ± 0.003

Table S8: UC sensitivity for β -NaYF₄ nanoparticles

Mn (%)	Measured $\frac{I_{ro}}{I_{go}}$	Fitted $\frac{I_{ro}}{I_{go}}$	Pressure sensitivity (% per GPa)	Absolute Pressure Sensitivity (per GPa)
0.0	1.153 ± 0.003	1.044 ± 0.023	-0.3 ± 1.4	-0.003 ± 0.017
0.5	1.431 ± 0.005	1.393 ± 0.016	-0.9 ± 0.6	-0.013 ± 0.009
1.5	2.776 ± 0.037	2.777 ± 0.050	-4.8 ± 1.5	-0.162 ± 0.040

Table S9: PL sensitivity for β -NaYF₄ nanoparticles

Mn (%)	Measured $\frac{I_{ro}}{I_{go}}$	Fitted $\frac{I_{ro}}{I_{go}}$	Pressure sensitivity (% per GPa)	Absolute Pressure Sensitivity (per GPa)
0.0	0.160 ± 0.000	0.165 ± 0.002	7.1 ± 0.7	0.011 ± 0.001
0.5	0.176 ± 0.002	0.172 ± 0.003	7.1 ± 1.3	0.012 ± 0.002
1.5	0.181 ± 0.003	0.178 ± 0.001	4.9 ± 0.6	0.008 ± 0.001

References

- (1) Zhang, Y.; Zhang, L.; Deng, R.; Tian, J.; Zong, Y.; Jin, D.; Liu, X. *Journal of the American Chemical Society* **2014**, *136*, 4893–4896.
- (2) Tian, G.; Gu, Z.; Zhou, L.; Yin, W.; Liu, X.; Yan, L.; Jin, S.; Ren, W.; Xing, G.; Li, S.; Zhao, Y. *Advanced Materials* **2012**, *24*, 1226–1231.
- (3) Wang, F.; Deng, R.; Liu, X. *Nature Protocols* **2014**, *9*, 1634–1644.
- (4) Yamaoka, H.; Zekko, Y.; Jarrige, I.; Lin, J.-F.; Hiraoka, N.; Ishii, H.; Tsuei, K.-D.; Mizuki, J. *Journal of Applied Physics* **2012**, *112*, 124503.
- (5) Mao, H.; Mao, W. L. *Treatise in Geophysics* **2007**, *2*, 231–267.
- (6) Mao, H.; Xu, J.-A.; Bell, P. *Journal of Geophysical Research: Solid Earth* **1986**, *91*, 4673–4676.
- (7) Henley, S.; Carey, J.; Silva, S. *Applied Physics Letters* **2004**, *85*, 6236–6238.
- (8) Wisser, M. D.; Chea, M.; Lin, Y.; Wu, D. M.; Mao, W. L.; Salleo, A.; Dionne, J. A. *Nano Letters* **2015**, *15*, 1891–1897.
- (9) Li, X.; Liu, X.; Chevrier, D. M.; Qin, X.; Xie, X.; Song, S.; Zhang, H.; Zhang, P.; Liu, X. *Angewandte Chemie* **2015**, *127*, 13510–13515.
- (10) Atkins, P. *Shriver and Atkins' Inorganic Chemistry*; Oxford University Press, USA, 2010.
- (11) Tu, D.; Liu, Y.; Zhu, H.; Li, R.; Liu, L.; Chen, X. *Angewandte Chemie International Edition* **2013**, *52*, 1128–1133.
- (12) Wang, F.; Liu, X. *Journal of the American Chemical Society* **2008**, *130*, 5642–5643.

- (13) Gargas, D. J.; Chan, E. M.; Ostrowski, A. D.; Aloni, S.; Altoe, M. V. P.; Barnard, E. S.; Sanii, B.; Urban, J. J.; Milliron, D. J.; Cohen, B. E. *Nature Nanotechnology* **2014**, *9*, 300–305.
- (14) Pawley, G. *Journal of Applied Crystallography* **1981**, *14*, 357–361.
- (15) Shannon, R. t. *Acta Crystallographica Section A: Crystal Physics, Diffraction, Theoretical and General Crystallography* **1976**, *32*, 751–767.
- (16) Shen, Y.; Kumar, R. S.; Pravica, M.; Nicol, M. F. *Review of Scientific Instruments* **2004**, *75*, 4450–4454.
- (17) Klotz, S.; Chervin, J.; Munsch, P.; Le Marchand, G. *Journal of Physics D: Applied Physics* **2009**, *42*, 075413.
- (18) Guo, Q.; Zhao, Y.; Mao, W. L.; Wang, Z.; Xiong, Y.; Xia, Y. *Nano Letters* **2008**, *8*, 972–975.
- (19) Wu, H.; Bai, F.; Sun, Z.; Haddad, R. E.; Boye, D. M.; Wang, Z.; Fan, H. *Angewandte Chemie International Edition* **2010**, *49*, 8431–8434.
- (20) Ragan, D. D.; Clarke, D. R.; Schiferl, D. *Review of Scientific Instruments* **1996**, *67*, 494–496.
- (21) Laporte, O.; Meggers, W. F. *Journal of the Optical Society of America* **1925**, *11*, 459–460.
- (22) Anderson, R. B.; Smith, S. J.; May, P. S.; Berry, M. T. *The Journal of Physical Chemistry Letters* **2013**, *5*, 36–42.
- (23) Berry, M. T.; May, P. S. *The Journal of Physical Chemistry A* **2015**, *119*, 9805–9811.
- (24) Liu, P.; Zhou, G.; Zhang, J.; Chen, S.; Yang, Y.; Wang, S. *Journal of Luminescence* **2013**, *144*, 57–63.

- (25) Chen, W.; Li, G.; Malm, J.-O.; Huang, Y.; Wallenberg, R.; Han, H.; Wang, Z.; Bovin, J.-O. *Journal of Luminescence* **2000**, *91*, 139–145.